Annals of Nuclear Energy 210 (2025) 110854

Contents lists available at ScienceDirect

Annals of Nuclear Energy

journal homepage: www.elsevier.com/locate/anucene

Transient behaviour and heat transfer characteristics in debris beds: Simulation and analysis of the LIVEJ2 experiment

Antonello Nappi [a,*], Marco Pellegrini [a], Shinya Mizokami [b], Koji Okamoto [a]

[a] Nuclear Professional School, Graduate School of Engineering, The University of Tokyo, 7-3-1 Hongo, Bunkyo-ku, Tokyo, 113-8656, Japan
[b] Tokyo Electric Power Company Holdings, Inc. (TEPCO), 1-1-3, Uchisaiwai-cho, Chiyoda-ku, Tokyo, 100-8560, Japan

ARTICLE INFO

Keywords:
Severe accident
CFD
Lower heat
Fukushima Daiichi nuclear power station
Porous media

ABSTRACT

Multiple uncertainties still exist about the state of the debris in Fukushima Daiichi Nuclear Power Station (1F). In the past, the attention of the nuclear safety community was focused on the heat transfer characteristics in the case of an homogeneous pool, but little attention was given to address the melting and heat transfer in the presence of a debris bed constituted of materials with different melting points. This condition represents a challenge for CFD analyses, because it includes multi-physics conditions, such as a low melting point fluid convecting into a debris bed surrounded by a crust on the vessel wall which has received little attention compared to classical CFD analyses. Even though a comprehensive analysis of a related experiment (i.e. LIVE-J2) has been performed recently by Madokoro et al. (2023) little attention on the results has been paid to the effect of debris bed porosity and the existence of a gap between the vessel wall and the crust. In the paper we have modified the porosity resistance based on the Ergun equation and proposed a simple model for the gap conductance in the lower part of the crust. The results show an improvement in the prediction of the thermal stratification and the vessel temperature in the lower locations. In addition, highlight that such phenomena constitute key parameters to keep into consideration in the simulation of prototypical cases both for CFD and lumped parameter codes (e.g. MELCOR, MAAP).

1. Introduction

The knowledge of distribution of fuel debris represents one of the most important information to achieve a successful decommissioning at the Fukushima Daiichi NPP. To do so, it is fundamental to be able to capture the thermal load of the lower head, which is influenced by the debris state inside the vessel at the time of failure. The thermal load in the case of the presence of a homogeneous pool was the subject of extensive research in the past, as experiment like BALI (Bonnet, 1999) or COPRA (Zhang et al., 2016) which focused on natural convection heat transfer in pools with internal heating. The results from these experiments were used to validate CFD codes, and different methodologies with different level of complexity were used, such as RANS (Sharma et al., 2022; Shams et al., 2020; Le Guennic et al., 2017; Sharma et al., 2022) and LES (Zhang et al., 2018). In the case of Fukushima Daiichi NPP, muon measurement (Yamashita et al., 2020) seem to indicate that a large part of the fuel debris still remains inside the lower head, indicating that the vessel failure may have occurred when the temperature of the corium pool was low enough so that the high melting oxides were still in a solid state (Sato et al., 2023). If the failure has occurred at such low temperatures, it is important to consider the oxidic and metallic phases separately, as a liquid metallic phase moving inside an oxidic porous bed. The issue of the thermal-hydraulics behaviour within particulate debris is also considered to be a topic of interest from the general nuclear safety community, with the SARNET network (W. Klein-Heßling et al., 2014) assigning it a high priority. In this scenario, the Late In-Vessel Phase Experiments (LIVE) (Madokoro et al., 2022, 2023) were conducted with the objective of reproducing such conditions. In the LIVE-J experiments, this was done by using two different simulant materials: an eutectic mixture of nitrate salts and ceramic beads (RIMAX) representing the low melting metallic phase and the oxidic phase respectively. Two subsequent experiments were conducted, under a cooperative agreement between the Karlsruhe Institute of Technology (KIT) and the Japan Atomic Energy Agency:

- LIVE-J1, focusing on the melting process of the solid nitrate salts
- LIVE-J2, exploring the formation and evolution of the molten pool in both steady state and transient conditions.

In this paper, the first two phases of the second experiment was the main focus of attention. Madokoro et al. (2023), performed CFD simulations for these same phases, using the software ANSYS FLUENT,

* Corresponding author.
E-mail address: antonellonappi@g.ecc.u-tokyo.ac.jp (A. Nappi).

https://doi.org/10.1016/j.anucene.2024.110854
Received 15 December 2023; Received in revised form 7 August 2024; Accepted 8 August 2024
Available online 22 August 2024

Table 1
Experimental phases characteristics.

Phase	Start/Stop [s]	Pool height [m]	Heating power [kW]	Cooling
1	0.0/20087	0.28	7	Yes
2	20087/28057	0.28	10	Yes

obtaining a good agreement with experimental data, although with several limitations: the results show a stronger thermal stratification then what could be seen in the experimental data, and a temperature peak is predicted for the lower elevations again not present in the experiment. Furthermore, Madokoro et al. perform a steady state simulation for these two phases, while later it will be demonstrated that this is not correct. In this paper, the authors aim to perform a fully unsteady simulation for both phases, while focusing on two aspects:

- effect of porous resistance on the convective motion inside the porous media,
- effect of gap conductance in the lower part of the pool,

aspects which were not analysed by the previous investigators. The results show an improvement with respect to the base case, highlighting the importance of both parameters when simulating convection inside porous media.

2. Experimental setup

Here a brief description only of the first two phases of the experiment is given, for a more detailed account, the interested reader may refer to Madokoro et al. (2023).

A summary of the conditions of phase 1 and 2 are given below:

- Phase 1: the initial solid mass of nitrate and RIMAX is heated with a constant power of 7 kW, while external cooling is supplied,
- Phase 2: the heating power is increased up to 10 kW.

The durations of each phase, as well as the other characteristics are summerized in Table 1.

3. Numerical methodology

Numerical simulation of the case was conducted using the commercial software STAR-CCM+ version 18.02.010. A similar setup to the one proposed by Madokoro et al. (2023) is used also in this case, meaning that only the vessel and pool are simulated, considering the rest of the structures as boundary conditions to the problem. Making use of the axisymmetric nature of the problem, all the simulations were performed using a 2D axisymmetric approximation, to reduce the computational load. This results in a mesh having one cell in the normal direction, with the difference in size between the cells near the axis and the one further being accounted in the solver. The mesh was generated using the automatic polyhedral mesh generator of STAR-CCM+. The mesh generated is shown in Fig. 1, and its main properties are discussed in Table 2. The characteristics of each mesh are reported in Table 2. The boundary condition for the temperature for the case are specified in Table 3 for each boundary and phase of the experiment. Convective heat transfer is considered for the external wall of the facility, the inner vessel-gas interface and the melt surface, where also radiative heat transfer is considered. The top part of the vessel is considered to be adiabatic. Since the simulations performed are unsteady, the convective BC use time varying reference temperatures, which are extracted from experimental values measured with thermocouples positioned in different parts of the experimental facility. For all gas-vessel interfaces an HTC of 10 W/m2/K is used, while for water-vessel interface the value of 500 W/m2/K is used. While the heat transfer coefficient along the external surface cannot be strictly considered as constant, its use is justified by the good agreement with experimental data obtained by Madokoro et al. (2023). Furthermore, the absence of geometrical information on the cooling system would introduce further uncertainties if the authors were to try to include it in the simulation. For the external wall of the vessel additionally, the temperature is considered to vary linearly from the bottom to the top of the vessel, with the bottom temperature corresponding to the inlet cooling water temperature, and the top corresponding to the outlet value, reflecting the experimental cooling loop configuration. For the interested reader, all the values of the reference temperatures, as well as the heat fluxes used for the simulation are reported in Appendix. The velocity boundary conditions were set to no slip for all the surfaces except the melt surface, where a slip boundary condition is set. The heat flux due to the heaters is fixed for each row of heaters depending on the experimental power draw. The thermal properties for the different materials are summarized in Table 4. Where indicated, in the Table 4, temperature dependent values are used. For the RIMAX and Nitrate properties, refer to Madokoro et al. (2022) and Bauer et al. (2011) respectively. For RIMAX, the conductivity used is not its physical value, as will be explained later. Since the range of temperatures considered is large, it is important to consider the change in thermophysical properties of the materials: in particular, for the nitrate, a polynomial expression is used for the density, and a variable heat capacity is considered, while for the RIMAX only a variation in the heat capacity is considered. The latent heat of fusion is considered as having a constant value of 100700 J/Kg. In STAR-CCM+, two different models are available to deal with the presence of porous media, which are denominated as superficial velocity and physical velocity formulations. In both approaches, the effect of the porous media on the flow is modelled by introducing sink terms into the momentum equation, which approximate the pressure losses due to the presence of the media itself. The two approaches differ as the physical velocity formulation takes into account the acceleration of the flow due to the restriction in the available area for the flow. In this case, the first approach was used, as the effect of this acceleration was considered to be negligible. For porous media, some relevant quantities must be defined before the discussion of the equations themselves: the porosity χ and tortuosity τ. The porosity of the media is defined as the ratio of the volume occupied by the fluid V_f and the overall cell volume V:

$$\chi = \frac{V_f}{V} \quad , \tag{1}$$

while the tortuosity is defined as the ratio of the actual path length through the porous media to the straight-line distance between the same two points. The definition of the latter is not relevant for this case, as it only affects the species transport. The continuity equation for a porous medium takes a different form.

$$\frac{\delta}{\delta t}\int_V \rho\chi\, dV + \oint_A \rho v_s \cdot dA = \int_V S_u\, dV \tag{2}$$

Where ρ is the density, and S_u represents explicit source terms. The velocity v_s appearing in Eq. (2) is the superficial velocity, defined as:

$$v_s = \chi \cdot v \tag{3}$$

where v is the physical velocity of the fluid. Using the superficial velocity takes into account the reduced cross-sectional area available for the fluid to pass through in the porous media. The term on the right hand side of the equal represents a user defined mass sink or source. The momentum equation again uses the surface velocity v_s instead of v, and takes the form:

$$\frac{\delta}{\delta t}\int_V \rho v_s\, dV + \oint_A \rho v_s \times v_s dA = \oint_A pI \cdot dA + \oint_A T \cdot da + \int_V f_b dV + \int_V f_p dV + \int_V S_u\, dV \tag{4}$$

Where p is the pressure, T is the stress tensor and f_b are the body forces. In Eq. (4), the term f_p represents the flow resistance, and it is calculated as the product of the porous resistance tensor P and the superficial

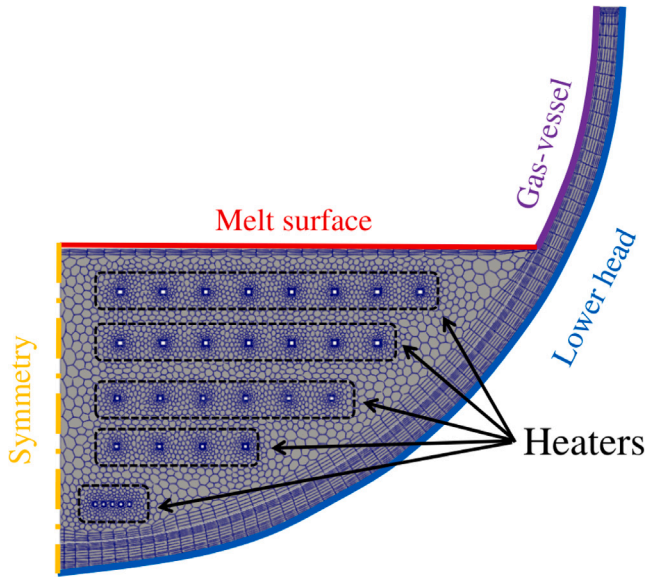

Fig. 1. Mesh used for the simulations performed.

Table 2
Grid properties.

Cell number	Max/Min cell dimension [m]	BL total thickness [m]
6.6k	0.05/1.25e−3	0.0125

Table 3
Boundary conditions for each phase. For all phases time dependent values are used for the reference temperatures.

Phase	Melt surface	Heaters	Lower head	Gas-Vessel
1	T_{rad}(t), $T_{conv,gas}$(t)	$\dot{Q}_{ph1}$	T_{conv,H_2O}(x,t)	$T_{conv,gas}$(t)
2	T_{rad}(t), $T_{conv,gas}$(t)	$\dot{Q}_{ph2}$	T_{conv,H_2O}(x,t)	$T_{conv,gas}$(t)

velocity v_s. The porous resistance tensor itself is further calculated as the sum of two components, a viscous term (P_v) which is linear and a quadratic inertial term (P_i):

$$P = P_v + P_i|v_s| \tag{5}$$

The evaluation of the two components of the this tensor was done using the Ergun equation (Ergun, 1952), which is widely applied for flow through porous media (Pang et al., 2021; Rankin et al., 1985). This leads to the evaluation of the two terms as:

$$P_v = A\frac{(1-\chi)^2}{\chi^3 d_p^2}\mu, \tag{6}$$

for the viscous term, and

$$P_i = B\frac{(1-\chi)}{\chi^3 d_p}\chi\rho, \tag{7}$$

for the inertial one. In Eq. (6), A is a constant (equal to 150), and χ, d_p and μ represent the porosity, particle diameter and dynamic viscosity of the fluid, respectively. The same quantities are used in Eq. (7), where B is again an experimental constant (equal to 1.75). Since the diameter of the ceramic beads ranged between 2.5 and 2.8 mm, the average value of 2.65 mm was used for this case.

The relative importance of the two terms can be evaluated by calculating the porous Reynolds number, defined as:

$$Re_p = \frac{\rho|\vec{U}|d_p}{\mu} \tag{8}$$

where d_p is the diameter of the particles making up the debris bed, in this case 0.00265 m. If Re_p is below 25 (Wood et al., 2020), in the Darcy regime, the flow can be well approximated by Stokes flow, meaning that the main contribution term is due to the viscous forces. As for all cases this is true, the viscous term will be the one which will be later reduced more to investigate its effect on the convective motion inside the debris pool. As for the energy equation, its form for a porous medium is again modified as:

$$\frac{\delta}{\delta t}\int_V \left(\chi(\rho E)_f + (1-\chi)(\rho c_p)_s T\right) dV + \oint_A \rho H v_s \cdot da = -\oint_A pI \cdot da + \oint_A T \cdot v_s da + \int_V f_b \cdot v_s dV + \int_V S_u dV \tag{9}$$

Where H is the enthalpy of the fluid. In Eq. (9), the porosity modifies both the time-dependent and transport term. Since one equation is used to describe the evolution of the temperature of both the solid and fluid phases, there is a necessity to introduce equivalent properties, which can represent the combined behaviour of the solid bed and of the fluid. This is done using an average on the porosity. For the conductivity, this leads to the definition of an equivalent conductivity (k_{eq}) as:

$$k_{eq} = \chi k_f + (1-\chi)k_s, \tag{10}$$

where, as for Eq. (9), the quantities with subscript f refer to fluid properties and s refer to solid properties. As Madokoro et al. noticed, the use of this average technique leads to non-physical values for the equivalent conductivity, and proposed the use of a lower value of the RIMAX conductivity, such that the averaged equivalent conductivity calculated with Eq. (10) returns a physically representative value. This leads to the use of a $k_{rimax} = 3.09$, lower than the physical value of 7.02. It is important to notice that sensitivity analysis performed by Villanueva et al. (2011) showed that the main parameter in determining the time of vessel failure is the material conductivity, therefore the modelling of this parameter is of primary importance.

Table 4
Material properties.

Material	Density [kg/m3]	C_p [J/kg/K]	k [W/m/K]	T_{melt} [C]
RIMAX	4018	C_p(T)	k_{RIMAX}	–
Nitrate	ρ(T)	C_p(T)	0.46	220
Stainless	8055	480	15.1	–

For the modelling of the melting process of the nitrate salts, STAR-CCM+ tracks the solid fraction of each cell explicitly from the temperature:

$$\alpha_s^* = \begin{cases} 1, & \text{if } T^* < 0 \\ f(T^*), & \text{if } 0 < T^* < 1 \\ 0, & \text{if } 1 < T^* \end{cases} \tag{11}$$

where T^* is the normalized temperature, defined as:

$$T^* = \frac{T - T_{solidus}}{T_{liquidus} - T_{solidus}} \quad . \tag{12}$$

As the nitrate salt mixture is eutectic, the liquidus and solidus temperatures coincide but the code assumes a small solidification interval equal to 0.002 K. This is done by STAR-CCM+ to improve the stability of the solution during the melting phase, and cannot be modified by the authors. In the case of a linear dependence between solid fraction and normalized temperature (as was for this case):

$$f(T^*) = 1 - T^* \quad . \tag{13}$$

Depending on the solid fraction, STAR-CCM+ allows the user to specify a flow stop condition, in the case that the solid fraction in a cell is over a certain value. In this case, the value of 0.5 was used, meaning that until the solid fraction drops below 0.5, no flow is allowed in a cell. Since in our case the solidification interval is very small, this parameter will not have a large effect on the simulation.

Regarding the discretization of the different operators, second order approximations for the convection of all quantities is used, and a

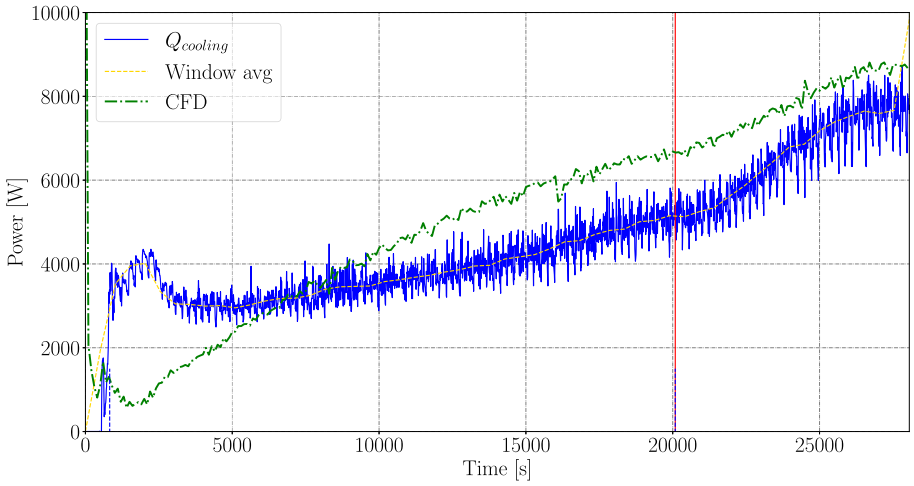

Fig. 2. Calculated cooling power, from experimental data. The red line corresponds to the start of phase 2. The calculated power through the crust from CFD is also reported in green.

Venkatakrishnan limited gradient discretization is used. As only the flow in the debris bed is analysed in the paper, and the diameter of the debris is small (2.65 mm), the flow is assumed to be approximated as Stokes flow, meaning that a laminar approximation can be used. The simulations were ran on a 16 cores machine (Ryzen 9 3950X), with a total CPU time of around 120k s each.

4. Results with preliminary model

As previously discussed, Madokoro et al. (2023) performed simulations for the first two phases using a steady state approximation. The cooling power extracted from the facility can be calculated employing the experimental data of the inlet and outlet temperatures and its flow rate. This analysis shows that the steady state approximation is not strictly valid, as it is presented in Fig. 2, where the cooling power is indeed increasing through both phases. Therefore, in this article unsteady simulations were performed, which allowed the authors to obtain the thermal transitory data. The thermocouples have been grouped depending on their location, to compare them with the experimental data. The groups are presented in Fig. 3. Before discussing the results, the expected behaviour of the pool under internal heating conditions is discussed. As the initially completely solid debris melts, a larger and larger molten pool will form, starting from the centre and moving towards the boundaries, where heat is extracted. As the pool grows larger, the molten nitrate is pushed upward by buoyancy, where it then loses heat to the atmosphere and descends along the vessel walls, to be reheated again and give rise to a large scale convective motion, which is expected to lead to a more uniform temperature field inside the debris bed. At the cooled vessel boundary also a thick crust remains, which provides an additional thermal isolation for the internal pool. As in this case the ceramic RIMAX material does not melt, the nitrate in the pool has to flow through this porous debris, which will hinder his motion, meaning that the transport due to large scale convection will be reduced in this case. This could lead to some thermal stratification, if the motion is reduced to the point where the mixing action of the large scale convection is reduced too much.

Now the time history data for the central thermocouples are presented in Fig. 4(a). The results show that the thermocouples high in the pool such as MT9 and MT21 show temperatures higher then the experimental values, while MT1 shows a better agreement. Keeping in mind the expected behaviour of the pool, it can be seen that the numerical simulations seem to predict an excess of thermal stratification, which could be due to a reduced convective mixing.

This thermal stratification can be seen also by looking at the temperature distributions at the end of phase 1 and 2 for the radial coordinates

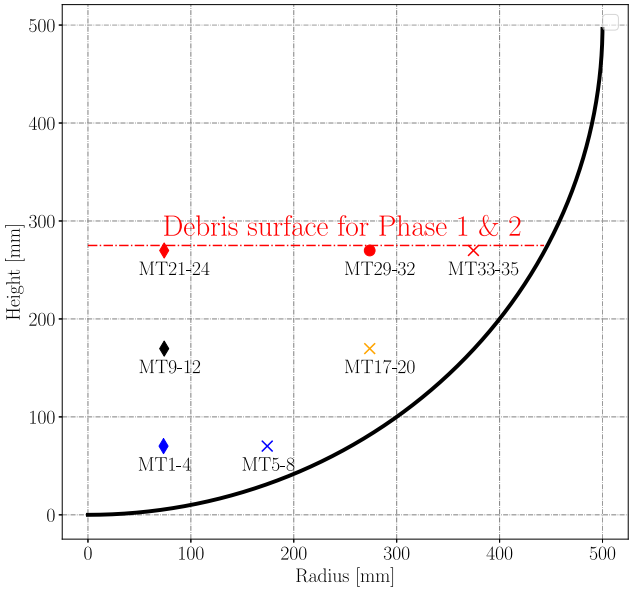

Fig. 3. Thermocouple groups considered for the analysis. Thermocouples sharing the same symbol or colour belong to the same group. The groups are: internal (diamond), vessel (cross), top surface (red) and bottom (blue). The red line represents the surface of the pool for phase 1 and 2.

R = 74 mm and R = 274 mm, shown respectively in Figs. 5(a) and 5(b). Thermal stratification is more pronounced for phase 2 than phase 1, due to the higher heating power in the second phase. Notice that this stratification is present in both the experiment and the simulations, meaning that even in the experiment the suppressive action of the RIMAX debris bed leads to a reduction in the overall flow motion which can lead to the experimentally seen peak in temperature in the upper pool.

The convective motion inside the pool does not only promote a better uniformity along the depth, but also in the radial direction (from the centre towards the vessel). As the motion is inhibited, this would lead to conditions where the dominant heat transfer mechanism near the boundaries is conduction, leading to a reduced heat transfer to the vessel. Now let us look at the vessel temperature profiles at the end of phase 1 and 2, shown in Figs. 6(a) and 6(b) respectively. At the end of phase 1, the simulation underestimates the heat flux to the vessel, leading to a reduced vessel temperature, while in phase 2, the vessel temperatures have a good agreement with the experiment.

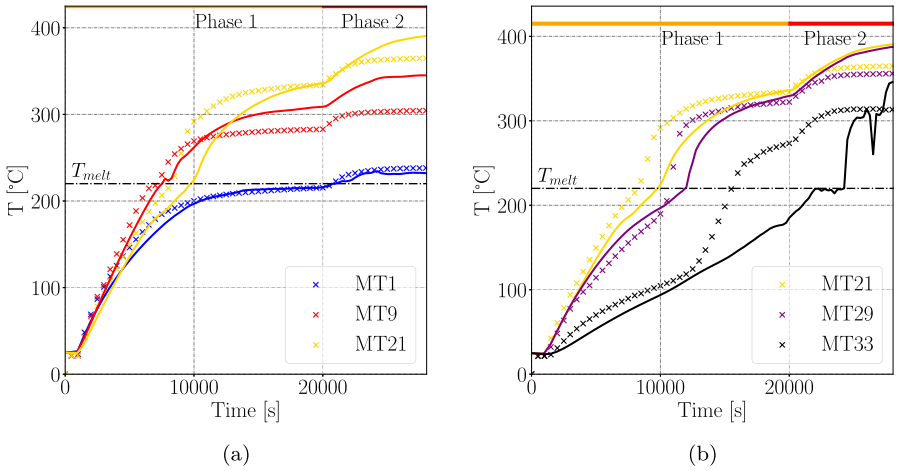

Fig. 4. Thermal transient data for the central group (a) and top group (b) thermocouples. Crosses refer to experimental data, while line refers to CFD results.

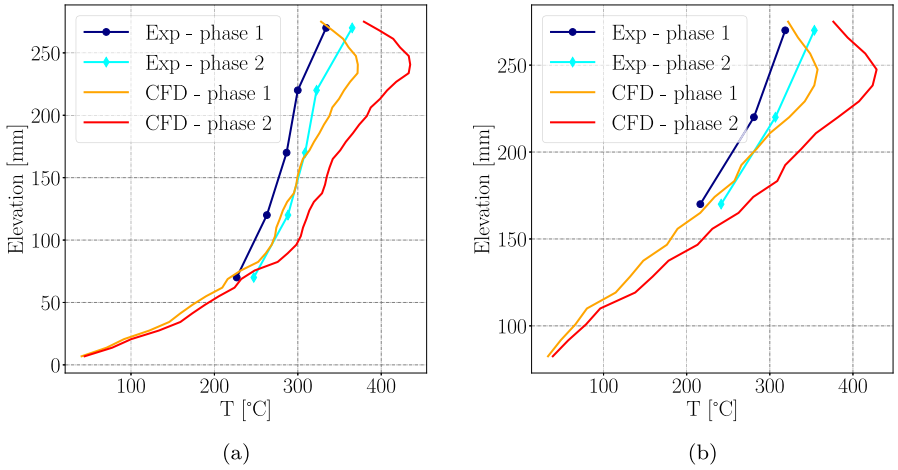

Fig. 5. Temperature results for end of phase 1 and phase 2. Elevation coordinate from the bottom of the pool. R = 74 mm (a) and R = 274 mm (b).

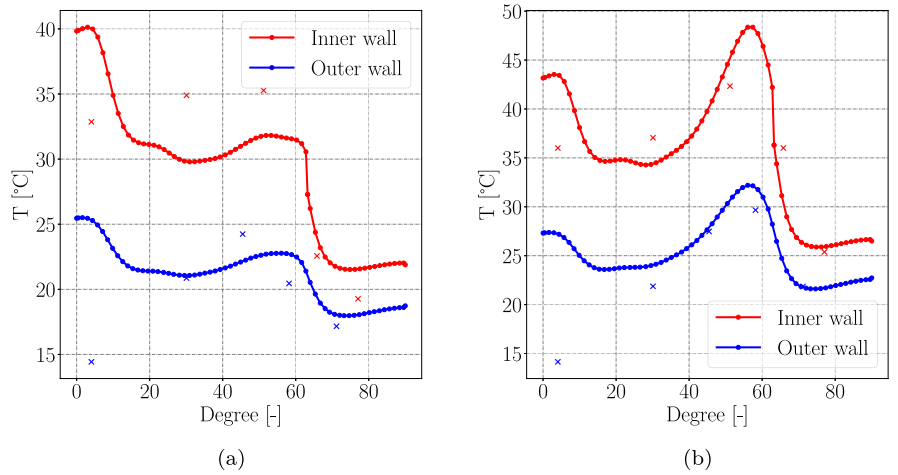

Fig. 6. Vessel wall temperature at the end of phase 1 (a) and 2 (b). Crosses refer to experimental data, while line refers to CFD results.

Considering that the heat flux through the crust is only conductive, it can be written:

$$\dot{Q}_{crust} = \frac{k_c}{t_c} \Delta T_{cv} \quad . \tag{14}$$

where k_c, t_c are crust conductivity and thickness, while ΔT_{cv} is the difference in temperature between the crust interface and the vessel. If the hypothesis that the temperature mismatch is due to the inhibition of the convective motion, the only way to obtain a similar heat flux to the experimental one is for the thickness of the crust to be smaller than the experimental value. Indeed, looking at the values of the crust thickness for both the end of phase 1 and 2, shown in Fig. 7, it can be seen how this is exactly the case, while for phase 1 where the crust thickness

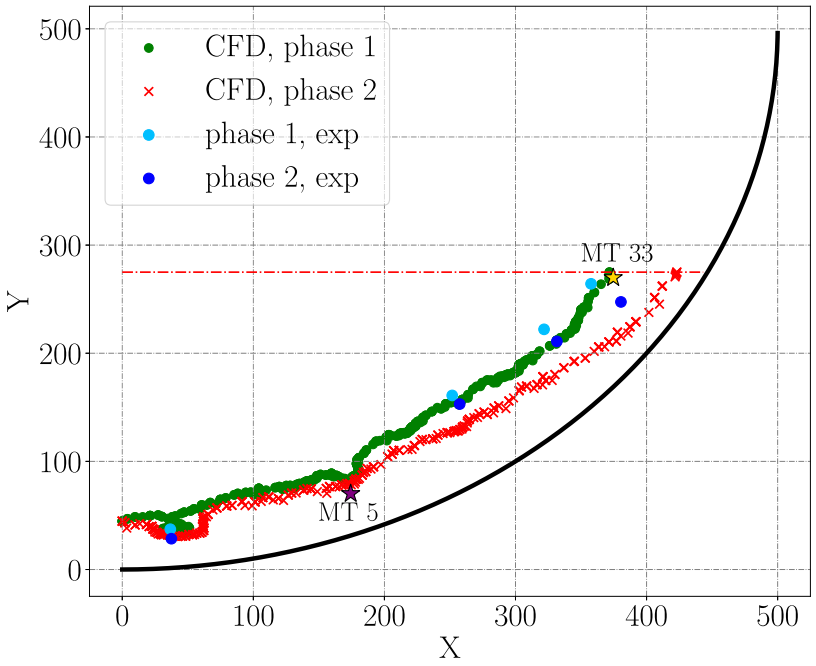

Fig. 7. Crust thickness for end of phase 1 and 2. The red dashed line corresponds to the surface of the pool.

is pretty similar to the experiment the heat flux is underestimated, leading to the underestimation of the vessel temperature. Another hint to the greater temperature disuniformity that exists in the simulation with respect to the experiment comes from Fig. 4(b). In particular, notice how experimentally MT33 at around 12500 s shows a change in temperature gradient while still below the melting point of nitrate. This change in gradient cannot be justified by an additional heat flux due to convective motion, as the nitrate is not molten. But it can be justified looking again at Eq. (14). As in the experimental case convection transports hotter nitrate towards the vessel, the crust near the thermocouple melts, causing the change in temperature gradient seen experimentally. Indeed in Fig. 7 it can be seen how at the end of phase 1 this thermocouple still lies inside the crust.

Considering again at the vessel temperatures for the end of phase 1 and 2 shown in Figs. 6(a) and 6(b), another important difference with the experimental results is the presence of a second peak at low elevations. In addition the temperature time data for the lower thermocouple group, shown in Fig. 8(a) shows how for MT5, which is located in the crust at the end of both phase 1 and phase 2, as it can be seen in Fig. 7, the temperature is underestimated with respect to experimental data. This is noticeable also when looking at the temperature distributions, as it is shown for H = 70 mm in Fig. 8(b), where for both phases the temperature appears underestimated, in contrast to what was seen previously for the other height coordinates.

In this region, the excessive heat transfer from the pool to the vessel explains the lower pool temperatures near the bottom and the overestimation of the vessel temperature. The cause of the excessive heat transfer might be the consequence of an overestimation of the thermal conductivity of the material in the lower part of the pool. The LIVE-J2 experiment indeed started from the solidified configuration achieved at the end of the LIVE-J1. As Madokoro et al. (2022) noticed, in the lower part of the vessel (̃20 mm from the bottom) at the end of the LIVE-J1 experiment the temperature is still below the melting point of the nitrate, meaning that when the experiment is started for phase 1 of LIVE-J2, in this region the solid nitrate beads are mixed with the RIMAX and possibly still air pockets may be present. This is in contrast with the rest of the bed, where nitrate melted and re-solidified, resulting in a direct contact between the two different materials. The expected effective conductivity in this region will be therefore lower, as it includes the presence of a mixture of RIMAX, nitrate salts and air that is trapped in the solid bed.

Table 5
Coefficients for the Ergun equations used in these simulations.

Simulation	A	B
Standard	150	1.75
Case 1	3	0.35
Case 2	10	1.17

5. Porosity model effects

As it was discussed previously, the excessive inhibition of the convective motion inside the pool could be the reason for the excessive thermal stratification seen in the CFD, as well as the slower than experimental radial spread of the pool. This could be due to two factors: an underestimation of the buoyancy force, which could be justified by the uncertainties in the constitutional relationship for nitrate or by an overestimation of the resistance. A sensitivity analysis was therefore performed modifying the coefficients of the Ergun equations for the inertial and viscous resistance component which influence the pressure drop in the debris bed. This way was pursued as various authors (Amiri et al., 2019; Jiang et al., 2002) also report that the constants of the Ergun equation need to be calculated empirically for different packed beds, depending on diameter distribution and packing. The modified values of the Ergun equation are reported in Table 5, where A is the coefficient for the viscous component and B for the inertial one. As previously discussed in the methodology section, the porous Reynolds number for these simulations fall into the Darcy regime, meaning that the viscous term will be the dominant one, and will be therefore reduced more in the two simulations performed.

Looking at Fig. 9(a), which shows the temperatures profile for the height of 220 mm at the end of phase 1, it can be seen how both models predict a faster lateral spreading of the pool, as the resistance of the flow is reduced. Case 1, with the lowest resistance, shows the largest spread, while Case 2 has a reduced spread, which is still higher than the Standard case, as its porous resistance is still higher. The enhanced mixing also means that the temperature profiles at radius 74 mm, shown in Fig. 9(b) for both Case 1 and 2 at the end of phase 1, show a lower temperature than the experimental one. This is to be expected, as more heat is being transferred due to convective motion

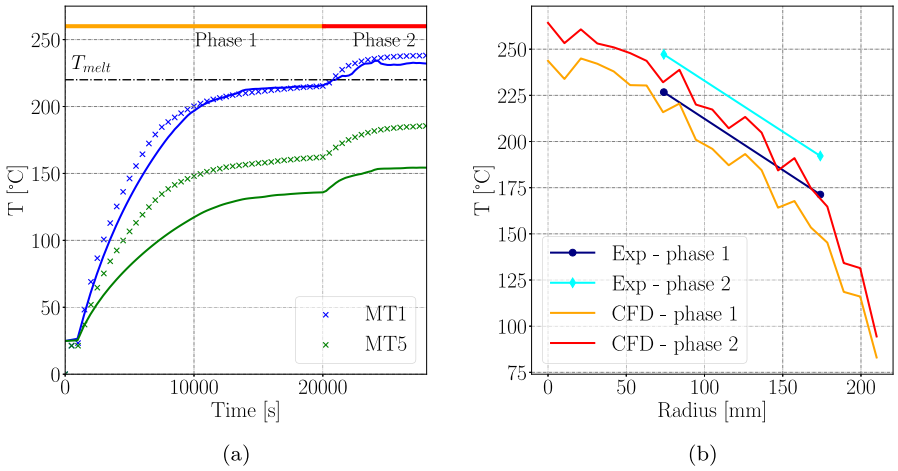

Fig. 8. Thermal transient for the lower thermocouples (a) and temperature results for end of phase 1 and phase 2 (b). For (a), line refer to CFD, crosses to experimental data. For (b), the radius coordinate starts from the centre of the pool. Height from the bottom is 70 mm.

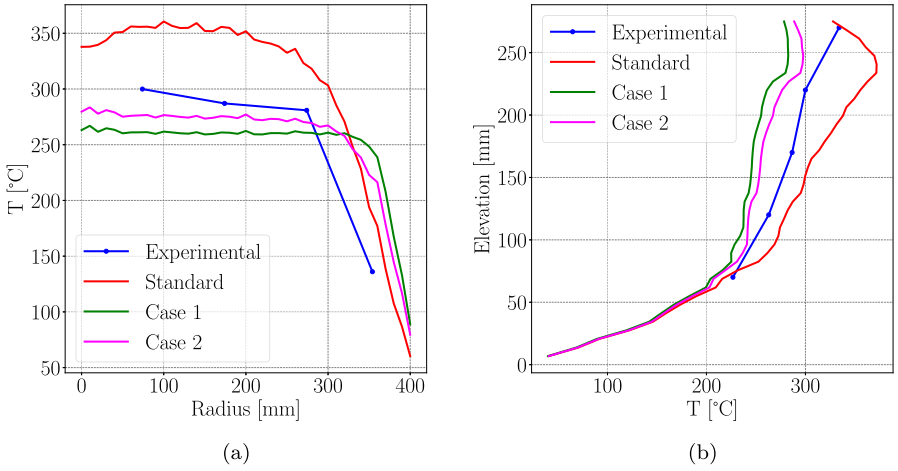

Fig. 9. Temperature results for end of phase 1. H = 220 mm (a) and R = 74 mm (b).

towards the walls and the upper surface of the pool, meaning that the overall heat losses will increase.

The lower convective motion inhibition leads to a better matching of the temperature profile for MT33, as shown in Fig. 10, where the temperature history data are shown. The change in gradient at 12500 s is captured, showing that it is indeed correlated to the lateral spreading of the pool. Notice that both Case 1 and 2 show similar results. Increase in lateral spreading of the pool has also an important effect on the vessel temperatures. In Fig. 11, the temperature for the three different cases are shown, and the effect of the higher lateral spreading is very noticeable as even for phase 1 now a temperature peak can be observed at around 55 deg, which gets more and more pronounced as the porous resistance is reduced.

The difference in the overall temperature field can be seen when comparing the temperature contours for the standard case and Case 1, as shown in Fig. 12, where also the velocity glyphs are reported. The standard case shows a much stronger thermal stratification, as previously discussed, while in Case 1 the temperatures are more uniform. In both cases convective motion is still present, but the magnitudes of the velocities due to buoyancy are one order of magnitude higher for Case 1 due to the lower porous resistance.

6. Lower pool thermal conductivity

As previously discussed, numerically a peak in the vessel temperature at low polar coordinates was associated with an excess of conductive heat flux from the last row of the heaters to the vessel. To test the hypothesis that a this is due to a higher thermal conductivity of the materials in the lower part of the pool, a final simulation was performed. This case, called Case 3, is a further evolution of Case 2, where a reduced material conductivity was applied in the lower part of the pool (~20 mm from the bottom), to reproduce the effects of the presence of air due to the incomplete melting of nitrate during the LIVE-J1 experiment. As for this case just verifying the effects of the model was necessary, a steady state simulation was performed, starting from the final state of the Case 2 simulation.

Table 6
Material properties used for the calculation of the equivalent conductivity.

Material	Conductivity [W/mK]
RIMAX Nitrate mix	2.22
Air	39.51e−03

To calculate the conductivity of the material in the lower part of the pool, the same method used to evaluate the equivalent conductivity of the nitrate and RIMAX mixture was used. In particular, one of the correlations summarized by Aichlmayr and Kulacki (2006) is used:

$$\eta = \frac{2\chi + \kappa(3 - 2\chi)}{3 - \chi + \kappa\chi} \tag{15}$$

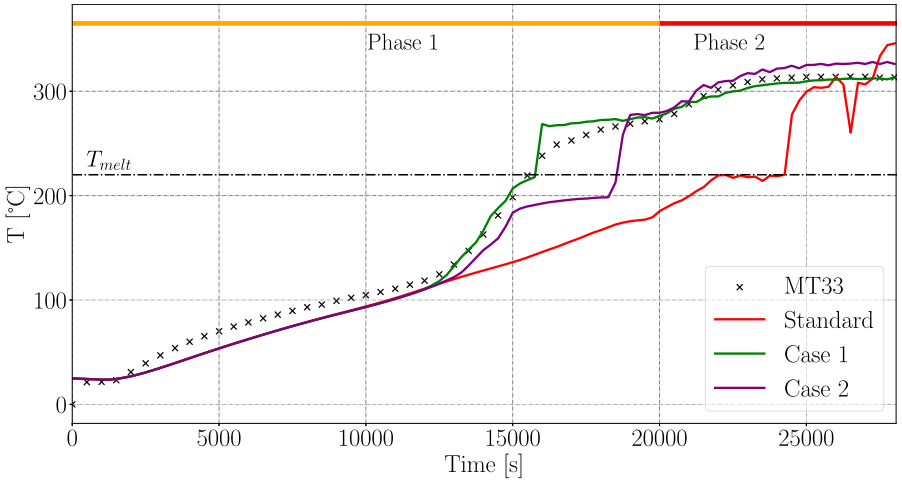

Fig. 10. Temperature profile for MT33 as a function of time. The crosses refer to experimental data, while the lines refer to CFD.

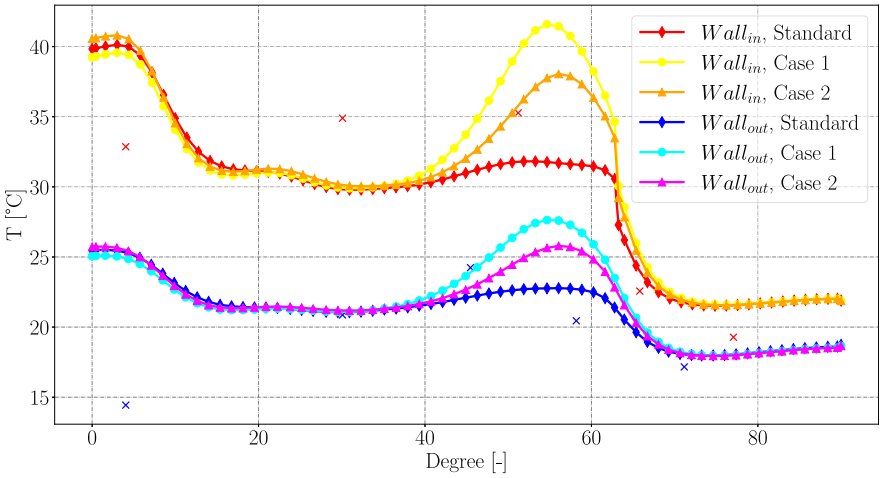

Fig. 11. Vessel temperature profile at the end of phase 1. The crosses refer to experimental data, while the lines refer to CFD.

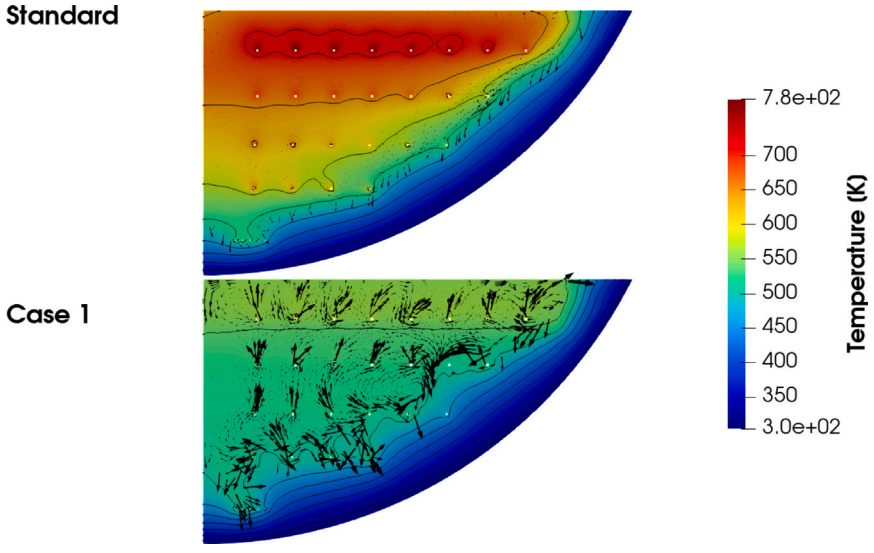

Fig. 12. Temperature contours and velocity glyphs for the end of phase 2. The glyph are scaled by the velocity magnitude.

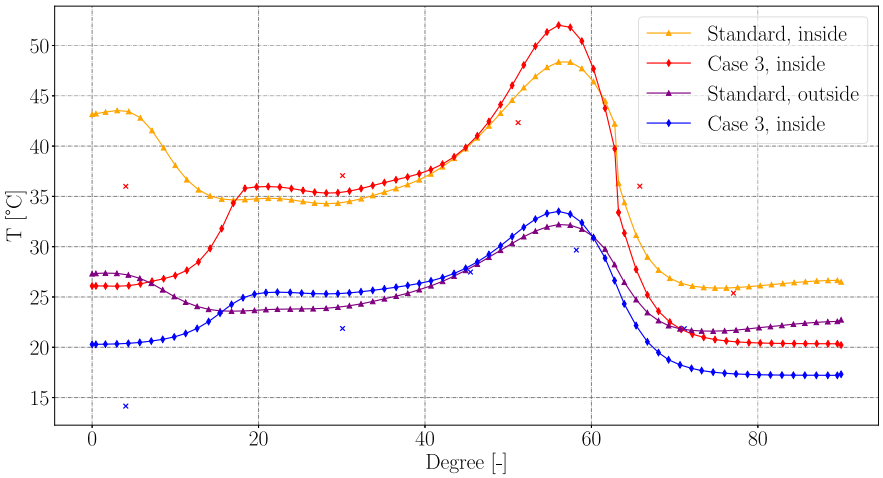

Fig. 13. Vessel wall temperature at the end of phase 2. Red colour refers to internal wall temperatures, blue to external ones. Both the standard and the Case 3 results are shown. Crosses refer to experimental data, while lines refer to CFD.

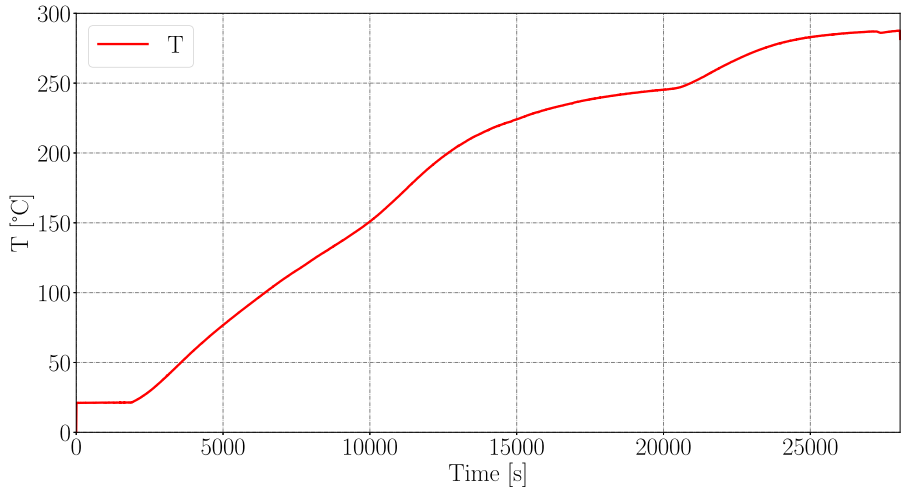

Fig. A.14. Gas/radiation BC temperature. Corresponding to thermocouple HT0i.

where η is the ratio of the effective to the fluid conductivity, χ is the porosity of the nitrate and RIMAX mixture which was experimentally evaluated being 0.423, κ is the ratio of the solid to the fluid conductivity. All the material properties used are listed in Table 6. For air, the conductivity at 220 °C and atmospheric pressure is used. For the RIMAX nitrate mixture, the equivalent conductivity calculated before is used. From η, the equivalent conductivity can be calculated, which is then used to assign a solid conductivity such that the value obtained from applying the mixing rule employed in the CFD simulation returns the same value. The equation for the solid conductivity to be used in the CFD becomes:

$$k_{s,CFD} = \frac{k_{eff} - \chi k_f}{1 - k_s} \tag{16}$$

Using the conductivity of air reported in Table 6, leads to a value of the solid conductivity $k_{s,CFD}$ of 0.2878 W/mK. As in this case the transitory is not of interest, a steady state simulation for phase 2 was performed. The wall temperature results are reported in Fig. 13, where it can be seen that the peak at the bottom of the vessel has changed into a temperature drop. The results in this region do not agree completely with the measured temperature due to the simplified analysis. A more detailed investigation of the problem is out of scope, but this analysis confirms the possibility of void gaps to be considered also in prototypical scenarios.

7. Conclusions

In this article, the first two phases of the LIVEJ-2 experiment (Madokoro et al., 2023) have been simulated using CFD. The use of an unsteady methodology allowed the authors to analyse both the initial thermal transient, when the nitrate is completely solid and the formation and enlargement of the convective pool. This phase is considered important as in the accident scenario early failure of the CRGT welds (Villanueva et al., 2011) could occur during the thermal transitory. At first an analysis is performed using a setup similar to the one proposed by Madokoro et al. (2023). The results show two main shortcomings:

- An excess of thermal stratification inside the pool.
- The presence of a peak in the vessel temperature at low elevations.

For the first point, the cause of this excess stratification was considered to be an excessive porous resistance inside the debris bed, leading to a reduced mixing inside the pool. This hypothesis was also supported by looking at the behaviour of one of the thermocouples (MT33) in the upper part of the pool, which experimentally showed a change in the thermal gradient attributed to the progressive thinning of the crust in the upper pool. To verify this, two simulations were performed with lower values of the porous resistance, which were obtained by

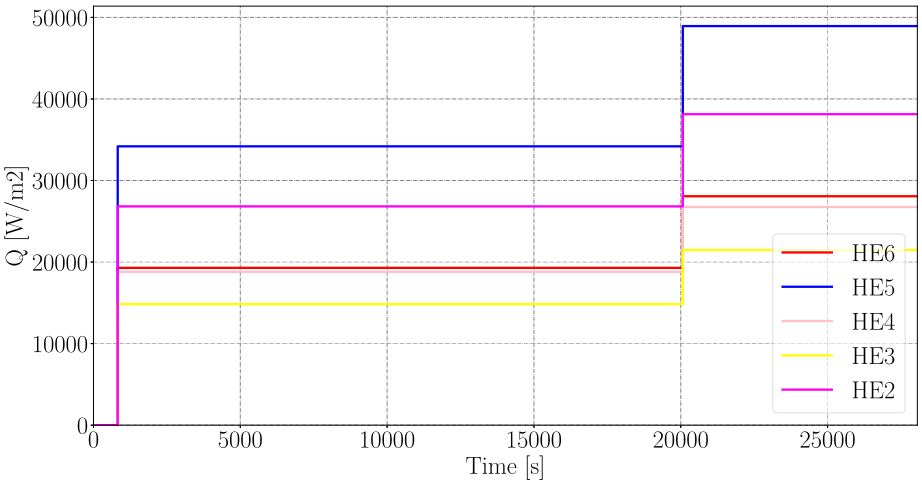

Fig. A.15. Heaters surface heat flux. HE 2 corresponds to the top row, HE 6 to the bottom row.

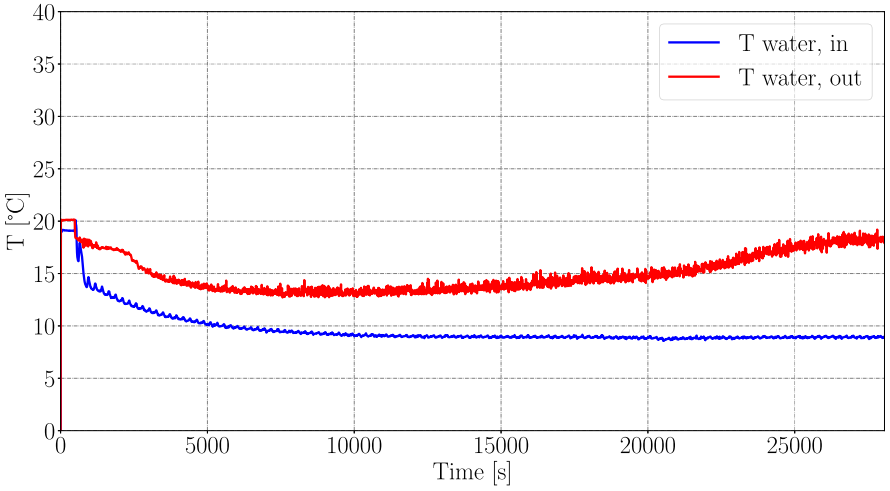

Fig. A.16. Cooling water temperature. Inlet is at the bottom of the vessel, outlet at the top.

reducing the constants in the Ergun equation. In both simulations, enhanced mixing led to a more uniform temperature inside the pool, which leads to a better agreement with the experimental data for the internal pool temperatures. The greater pool mobility also means that a quicker radial expansion of the pool during phase 1 is predicted, which enables to reproduce the experimental behaviour of the MT33 thermocouple. The faster radial expansion also led to a higher heat flux towards the vessel, meaning that for both simulations the temperatures in the upper part of the vessel at the end of the first phase increase with respect to the base case. To tackle the second point, the prediction of the higher temperature at low elevation is associated with conduction from the lowest row of heaters to the vessel. However, as hypothesized by Madokoro et al. (2022) the lower region might contain air trapped between the crust and the vessel resulting in a lower thermal conductivity. The results of the analysis confirm this assumption. This work confirms the ability for the employed CFD model to predict correctly the temperature evolution in a debris bed of a given porosity. Hence it could be used to extrapolate more prototypical conditions such as oxidic and metallic debris accumulated in the lower head during the Fukushima Daiichi accident. In addition it identifies key uncertain parameters to take into account for uncertainty analysis, such as the effect of porosity as well as the possibility of gaps between the crust and the vessel.

CRediT authorship contribution statement

Antonello Nappi: Writing – original draft, Visualization, Software, Methodology, Formal analysis. **Marco Pellegrini:** Writing – review & editing, Supervision, Funding acquisition. **Shinya Mizokami:** Funding acquisition. **Koji Okamoto:** Funding acquisition.

Declaration of competing interest

The authors declare that they have no known competing financial interests or personal relationships that could have appeared to influence the work reported in this paper.

Data availability

The authors do not have permission to share data.

Acknowledgements

This research was carried out thanks to research funding provided by Tokyo Electric Power Company Holdings. Inc. In addition, vital support for the measurements and boundary conditions has been provided by Yamashita Takuya of JAEA/CLADS. The authors thanks both groups for their invaluable support.

Appendix. BC

In this section, the temperatures as well as other data used as BC for the simulations are presented for the interested reader (see Figs. A.14–A.16).

References

Aichlmayr, H.T., Kulacki, F., 2006. The effective thermal conductivity of saturated porous media. Adv. Heat Transf. 39, 377–460.

Amiri, L., Ghoreishi-Madiseh, S.A., Hassani, F.P., Sasmito, A.P., 2019. Estimating pressure drop and Ergun/Forchheimer parameters of flow through packed bed of spheres with large particle diameters. Powder Technol. 356, 310–324.

Bauer, T., Laing, D., Tamme, R., 2011. Overview of pcms for concentrated solar power in the temperature range 200 to 350 C. Adv. Sci. Technol. 74, 272–277.

Bonnet, J., 1999. Thermal hydraulic phenomena in corium pools: the bali experiment.

Ergun, S., 1952. Fluid flow through packed columns. Chem. Eng. Prog. 48 (2), 89, URL https://cir.nii.ac.jp/crid/1572261550410403712.

Jiang, Y., Khadilkar, M., Al-Dahhan, M., Dudukovic, M., 2002. Cfd of multiphase flow in packed-bed reactors: I. k-fluid modeling issues. AIChE J. 48 (4), 701–715.

Le Guennic, C., Saas, L., Le Tellier, R., Wu, Y., Guingo, M., Laviéville, J., 2017. Contribution of cfd studies to ivr assessment. In: 8th European Review Meeting on Severe Accident Research-ERMSAR-2017. Warsaw, Poland.

Madokoro, H., Yamashita, T., Gaus-Liu, X., Cron, T., Fluhrer, B., Sato, I., Mizokami, S., 2023. The experimental and simulation results of live-j2 test—investigation on heat transfer in a solid–liquid mixture pool. Nucl. Technol. 209 (2), 144–168. http://dx.doi.org/10.1080/00295450.2022.2121545.

Madokoro, H., Yamashita, T., Sato, I., Gaus-Liu, X., Cron, T., Fluhrer, B., Stängle, R., Wenz, T., Vervoortz, M., 2022. Live-j1 experiment on debris melting behavior toward understanding late in-vessel accident progression of the fukushima daiichi nuclear power station. In: Vortrag Gehalten Auf 19th International Topical Meeting on Nuclear Reactor Thermal Hydraulics. NURETH-19 2022, Brüssel, Belgien, pp. 6–11, März 2022.

Pang, M., Zhang, T., Meng, Y., Ling, Z., 2021. Experimental study on the permeability of crushed coal medium based on the ergun equation. Sci. Rep. 11 (1), 23030. http://dx.doi.org/10.1038/s41598-021-02524-4.

Rankin, W., Roller, P., Batterham, R., 1985. Analysis of the permeability of granulated iron sinter feeds using the ergun equation. Min. Metall. Explor. 2 (53), 59. http://dx.doi.org/10.1007/BF03402597.

Sato, I., Yoshikawa, S., Yamashita, T., Cibula, M., Mizokami, S., 2023. Maap code analysis focusing on the fuel debris condition in the lower head of the pressure vessel in Fukushima–Daiichi nuclear power station unit 2. Nucl. Eng. Des. 404, 112–205.

Shams, A., Dovizio, D., Zwijsen, K., Le Guennic, C., Saas, L., Le Tellier, R., Peybernes, M., Bigot, B., Skrzypek, E., Skrzypek, M., et al., 2020. Status of computational fluid dynamics for in-vessel retention: Challenges and achievements. Ann. Nucl. Energy 135, 107004.

Sharma, A.K., Pellegrini, M., Okamoto, K., Furuya, M., Mizokami, S., 2022. Validation and application of numerical modeling for in-vessel melt retention in corium pools. Int. J. Heat Mass Transfer 196, 123313.

Villanueva, W., Tran, C.T., Kudinov, P., 2011. Assessment with coupled thermo-mechanical creep analysis of combined crgt and external vessel cooling efficiency for a bwr.

W. Klein-Heßling, W., Sonnenkalb, M., Jacquemain, D., Clément, B., Raimond, E., Dimmelmeier, H., Azarian, G., Ducros, G., Journeau, C., Puebla, L.H.e.A., 2014. Conclusions on severe accident research priorities. Ann. Nucl. Energy 74, 4–11. http://dx.doi.org/10.1016/j.anucene.2014.07.015, ERMSAR 2013 conference of the SARNET network.

Wood, B.D., He, X., Apte, S.V., 2020. Modeling turbulent flows in porous media. Annu. Rev. Fluid Mech. 52, 171–203.

Yamashita, T., Sato, I., Honda, T., Nozaki, K., Suzuki, H., Pellegrini, M., Sakai, T., Mizokami, S., 2020. Comprehensive analysis and evaluation of Fukushima Daiichi nuclear power station unit 2. Nucl. Technol. 206 (10), 1517–1537. http://dx.doi.org/10.1080/00295450.2019.1704581.

Zhang, L., Luo, S., Zhang, Y., Tian, W., Su, G., Qiu, S., 2018. Large eddy simulation on turbulent heat transfer in reactor vessel lower head corium pools. Ann. Nucl. Energy 111, 293–302.

Zhang, L., Zhang, Y., Zhao, B., Ma, W., Zhou, Y., Su, G., Tian, W., Qiu, S., 2016. Copra: a large scale experiment on natural convection heat transfer in corium pools with internal heating. Prog. Nucl. Energy 86, 132–140.